ARTICLE IN PRESS

Extreme Mechanics Letters ▮ (▮▮▮▮) ▮▮▮–▮▮▮

Contents lists available at ScienceDirect

Extreme Mechanics Letters

journal homepage: www.elsevier.com/locate/eml

Uniform tensile elongation in Au–Si core–shell nanowires

Julien Godet [a,*], Clarisse Furgeaud [a], Laurent Pizzagalli [a], Michael J. Demkowicz [b]

[a] Institut Pprime, CNRS UPR 3346, Université de Poitiers, F-86962 Futuroscope Chasseneuil, France
[b] Materials Science and Engineering, Texas A&M University, College Station, TX 77843, USA

ARTICLE INFO

Article history:
Received 30 November 2015
Accepted 28 March 2016
Available online xxxx

Keywords:
Plasticity
Dislocation
Nanostructure
Simulation
Amorphous silicon
Gold

ABSTRACT

In order to evaluate the role of a hard amorphous silicon (*a*-Si) shell on the deformation of a soft crystalline gold core, we investigated the mechanical properties of the Au@*a*-Si core–shell nanowire (NW) by using molecular dynamics simulations. We first optimized an existing parametrization of the MEAM potential to better reproduce the mechanical properties of gold and silicon as well as Au–Si interactions. The comparison of the tensile tests performed on pristine Au NW, *a*-Si shell and Au@*a*-Si core–shell NW revealed that the hard amorphous shell works against the growth of the ledges left by localized plasticity. In consequence, the localized plasticity and the expansion of nano-twin are reduced. A homogeneous plastic deformation of the core–shell was then observed at almost a constant flow stress equal to the yield stress. This behavior is characteristic of an elastic-perfect plastic material.

1. Introduction

The narrow link between the strength and the density of materials observed in the Ashby diagram [1] shows a near linear proportionality between both properties. This observation questionned the possibility to fill empty areas in this diagram in order to build hard materials with low density. Architectured materials have been proposed to solve this problem [2], in particular with architectures based on several length scales to mimic nature [3,4].

Metal nano-foams are one possible high strength-to-weight ratio architecture but they often have low thermal stability. Biener et al. [5] showed that a thin layer of hard amorphous oxide can stabilize the foam in temperature and increase the hardness and the Young's modulus of the foam. The goal of our study was to investigate the mechanical stability of the core–shell nanowires (NWs) composed of a soft core and a hard amorphous shell as models for the Au foam ligaments covered by amorphous oxide.

Ideal shear strength gives an estimate of the stress needed to homogeneously nucleate a dislocation dipole in bulk. We considered gold for the crystalline core for its low ideal shear strength (1.66 GPa [6]) and silicon for the hard shell for its large ideal shear strength (13.7 GPa [7]). We took amorphous silicon for the shell because it is easier to simulate than amorphous silica.

To investigate the onset of plasticity in such core–shell structures, we used molecular dynamics simulations. We focused on Modified Embedded Atom Method (MEAM) potentials for their ability to model compact structures like FCC as well as open structures like cubic diamond with a relatively high efficiency in CPU time. Recently, a new MEAM parametrization for Au–Si alloys has been optimized to reproduce thermodynamics properties including the phase diagram [8] but the mechanical properties are not optimal. Here, we considered the parametrization of Lee et al. for gold [9] and silicon [10] that we further optimized in order to get improved description of mechanical properties.

* Corresponding author.
E-mail address: julien.godet@univ-poitiers.fr (J. Godet).

http://dx.doi.org/10.1016/j.eml.2016.03.023
2352-4316/

Please cite this article in press as: J. Godet, et al., Uniform tensile elongation in Au–Si core–shell nanowires, Extreme Mechanics Letters (2016), http://dx.doi.org/10.1016/j.eml.2016.03.023

In this work, we present our fitted potential for pure silicon and pure gold, and we compare Si–Au interfaces when silicon is crystalline or amorphous. Furthermore, we performed tensile tests on pristine Au NW, Au@*a*-Si core–shell NW and empty *a*-Si shell to understand the influence of a hard amorphous shell on the mechanical properties of a soft crystalline core and explain our findings.

2. Methods

2.1. Simulation setup

The simulations were performed with the molecular dynamics (MD) code LAMMPS [11]. Gold and silicon interactions were modeled with the MEAM potentials described in the next section. We optimized the time steps to 0.5 fs. The deformations were done at a strain rate of 5.10^8 s^{-1}, typical of MD simulations. Periodic boundary conditions were applied in all simulations. Static minimization was performed with a conjugate gradient algorithm until atomic forces are smaller than 10^{-6} eV/Å. For MD simulations we considered the NVT ensemble to control the NW deformations. The temperature was controlled by the Nosé–Hoover thermostat [12,13] with the 'thermal mass' parameter set such that the characteristic time for temperature fluctuation is $\tau_T = 50$ fs in all simulations.

2.2. Potential optimization for pure Au and pure Si

We initially considered the MEAM parametrization of Lee et al. for gold [9] and silicon [10]. Those parametrizations involve the second nearest-neighbor formalism of the MEAM potential. However, Lee et al. chose a $C_{\min}$ parameters greater than 1.0 for gold and higher than 0.5 for silicon, which turns off the second nearest-neighbor formalism. The $C_{\min}$ parameter controls the way a neighbor atom can screen an interatomic interaction in the evaluation of the potential energy (see [14] for details). Here, we took $C_{\min} = 0.5$ for silicon and $C_{\min} = 0.8$ for gold but we subsequently considered the first nearest-neighbor formalism because the improvements obtained by the second nearest-neighbor formalism are not pertinent for gold [9] and silicon [10]. The MEAM parameters file for the LAMMPS code is given in the Supplementary material (see Appendix A).

2.2.1. Optimization of the mechanical properties

Table 1 gives some of the physical properties calculated with this potential. Firstly, the elastic constants were all very close to the experimental values. In particular the silicon ⟨110⟩{111} shear modulus (62 GPa) was better reproduced in comparison with the initial MEAM parametrization [14] and with some common potentials such as Stillinger–Weber's [15] or Tersoff's [16]. The cohesive energy, the lattice parameter and the bulk modulus were used as input parameters in the MEAM potentials, they are then well described.

The ability of a potential to reproduce the dislocation-mediated plasticity is usually estimated by the calculation of the generalized stacking fault energy (GSFE) in the slip plane of a dislocation along its Burgers vector. The definition was first given by Vitek [24]. In order to improve the unstable stacking fault energies along the ⟨110⟩ in the {111} shuffle set plane of silicon, the $C_{\min}$ parameter of Si was decreased to 0.5. The height of this barrier is indirectly related to the energy required to move a dislocation from one Peierls Valley to the other through the Peierls–Nabarro model. In addition to this, the $C_{\max}$ parameter was increased to 3.85 to smooth the GSFE curve. For similar reasons, the $C_{\min}$ parameter was changed to 0.8 in gold but unfortunately, the intrinsic stacking fault energy remained slightly too high at 0.041 J/m^2 in comparison with the experimental value of 0.032 J/m^2. In consequence, smaller dissociation distances between the two partial dislocations in gold are expected.

The ideal shear strength corresponds to the maximum of the derivative of the GSFE curve with respect to the displacement along the Burgers vector. It gives an estimate of the stress required to homogeneously nucleate a dislocation dipole in bulk. Our computed value for silicon in the {111} plane of the shuffle set (13.8 GPa) was consistant with the 13.7 GPa DFT value. It was slightly too high for gold (1.75 GPa) compared to 1.66 GPa in DFT and could lead to an overestimation of the yield point.

The ideal tensile strength represents the minimum normal stress for a plane to cleave a crystal along this plane (see Kang et al. [7] for more details). The original parametrization of Lee et al. for silicon [10] gave a too high value (greater than 80 GPa) due to an abrupt cut off function of the potential. More recently, the same authors proposed a version with a larger cut off and an increase of the length of the truncation region to reproduce the *ab initio* value [25]. However, this modification implies a drastic increase of the number of neighbors for the energy evaluation, leading to a potential with an increased computational cost. To limit the CPU time, we observed that an increase of the length of the truncation region from 0.1 to 2.1 Å ('*delr*' parameter in supplementary materials (see Appendix A)) without modifying the cut off distance allows to match the DFT value of the ideal tensile strength. However, this parameter is not independent for silicon and gold in the code LAMMPS and we had then to limit its value to 1.5 Å to avoid an unexpected surface reconstruction of gold. As a result, the ideal tensile strength was 31 GPa as opposed to a 23 GPa DFT value (Table 1) but the results of our study about the plasticity of gold should not be affected by this problem due to gold being softer than silicon.

2.2.2. Optimization of other physical properties

The calculated surface energies of gold and silicon are reported in Table 1. The energies of gold {110} and {111} surfaces are close to the DFT values, but the {100} surface energy is largely underestimated compared to DFT. Nevertheless, the lowest energy surface is {111} and the highest {100} as expected. For silicon the errors are less than 20%, which is very typical when the potentials are not adjusted on the surface properties. The error of surface energies could modify the results for the systems with the smallest diameter (less than 5 nm) when the surfaces are predominant with respect to the bulk (see for example the variation of the Young's modulus in small Si NW [26]).

Please cite this article in press as: J. Godet, et al., Uniform tensile elongation in Au–Si core–shell nanowires, Extreme Mechanics Letters (2016), http://dx.doi.org/10.1016/j.eml.2016.03.023

Table 1
Physical properties calculated for pure Au and pure Si with the optimized version of MEAM (this work). For comparison the experimental values labeled * and the DFT values are given. The C_{ij} are the cubic elastic constants, B the bulk modulus, μ the shear modulus, E_c the cohesive energy, a_0 the equilibrium lattice constant, γ^{us} the unstable stacking fault energy, γ^{is} the intrinsic stacking fault energy, τ the ideal shear strength, σ_c the ideal tensile strength, E_{surf} the surface energies, E_{subst} the energy of substitutional atom. For silicon, the γ^{us}, γ^{is}, τ and $E_{surf}^{(111)}$ values are calculated in the shuffle set plane.

	Au (MEAM)	Au (exp*/DFT)	Si (MEAM)	Si (exp*/DFT)
C_{11} (GPa)	202	202* [17]	169	167* [17]
C_{12} (GPa)	171	170* [17]	65	65* [17]
C_{44} (GPa)	46	45* [17]	84	81* [17]
B (GPa)	181	180* [17]	99	99* [17]
μ ⟨110⟩{111} (GPa)	26	26* [17]	62	61* [17]
E_c (eV/atom)	3.93	3.93* [18]	4.63	4.63* [19]
a_0 (Å)	4.07	4.08* [19]	5.43	5.43* [19]
γ^{us} ⟨110⟩{111} (J/m^2)			1.60	1.67 [20]
γ^{us} ⟨112⟩{111} (J/m^2)	0.106	0.092 [6]		
γ^{is} ⟨112⟩{111} (J/m^2)	0.041	0.032* [21]		
τ ⟨110⟩{111} (GPa)			13.8	13.7 [7]
τ ⟨112⟩{111} (GPa)	1.75	1.66 [6]		
σ_c ⟨110⟩ (GPa)			31	23 [7]
$E_{surf}^{(100)}$ (2 × 1 for Si) (J/m^2)	1.08	1.97 [6]	1.69	1.45 [22]
$E_{surf}^{(110)}$ (J/m^2)	1.05	1.10 [6]	1.84	1.70 [22]
$E_{surf}^{(111)}$ unreconstructed (J/m^2)	0.90	0.917 [6]; 1.54(poly)* [23]	1.53	1.74 [22]
$T_{melting}$ (K)	1230–1330	1337 [18]	2430	1687 [18]
$E_{subst}^{Si\ in\ Au}$ (eV/atom)			0.64	0.63 [6]
$E_{subst}^{Au\ in\ Si}$ (eV/atom)	1.84	1.55 [6]		

While the melting temperature of gold is well described by the potential, the melting temperature of silicon (about 2430 K) is far from the experimental value of 1687 K. However the mechanical tests in this work are performed at temperatures below the melting temperature of gold, then well below the melting temperature of silicon. The too high melting temperature of silicon should then not affect our results on mechanical properties in Au@Si core–shell NW.

The Radial Distribution Function (RDF) of the Si amorphous phase (see Section 3.1 for preparation details) has been calculated to evaluate the ability of the potential to describe this phase (not shown here). We observed a better reproduction of the experimental RDF [27] by decreasing the $C_{\min}$ parameters to 0.5. In particular, the artificial small peak located just before the second nearest-neighbor peak of the RDF given by the original MEAM potential is removed. However, the density of *a*-Si equal to 2.336 g/cm^3 is slightly overestimated compared to the experimental value of 2.289 g/cm^3 [28]. The *a*-Si phase obtained with the optimized MEAM potential is characterized by an energy of 0.301 eV/atom higher than in the crystalline phase. This energy difference is about 3 or 4 times higher than the experimental value [29] probably due to the fast quenching rate used in molecular dynamics simulations.

2.3. Optimization of the Au–Si interactions

The Au–Si interactions have been adjusted on the lattice parameter, the cohesive energy and the bulk modulus of the metastable B1 phase of Au–Si (NaCl structure) calculated in DFT-LDA by Ryu et al. [8] (Table 2). The cross parameters listed in the Supplementary material (see Appendix A) come from the MEAM optimization of Ryu et al. [8]. In addition, the ratio of the electronic densities ρ_{Au}/ρ_{Si} has been optimized with respect to the energies of the substitutional atom. Table 1 shows a very good agreement for the substitutional Si atom in pure Au, but the energy of the substitutional Au atoms in pure Si is overestimated by about 0.3 eV/atom. This overestimation may lead to an artificial increase of the energy of the gold–silicon interactions. However, the comparison of the physical properties calculated with our MEAM potential and with the DFT method [8] for the $L1_2$ phase of Au_3Si (Table 2) shows a relatively good agreement, without any optimization, supporting the relatively good parametrization of the Au–Si interactions. At this point, we think that our optimized version of the MEAM potential should be good enough to model the mechanical properties in Au@*a*-Si core–shell NW.

Table 2
Comparison between MEAM (this work) and DFT calculated physical properties [8] for B1 and $L1_2$ structures of Au–Si alloys. a_0 is the lattice parameter, E_c the cohesive energy, B the bulk modulus, C_{11} the elastic constant.

	AuSi (B1)		Au_3Si ($L1_2$)	
	DFT	MEAM	DFT	MEAM
a_0 (Å)	5.184	5.2	4.055	4.113
E_c (eV/at)	4.155	4.155	3.945	3.921
B (GPa)	127	127	152	144
C_{11} (GPa)	303	387	159	148

3. Model systems

This work focuses on the mechanical properties of core–shell NWs composed of a soft core covered with a hard shell. The amorphous silicon was chosen as a surrogate of hard shell. Here, we first describe the preparation

Please cite this article in press as: J. Godet, et al., Uniform tensile elongation in Au–Si core–shell nanowires, Extreme Mechanics Letters (2016), http://dx.doi.org/10.1016/j.eml.2016.03.023

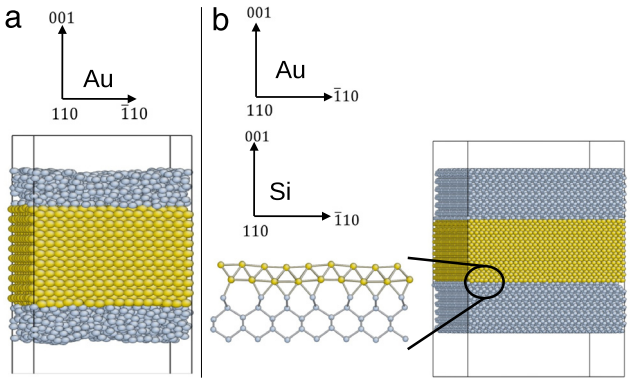

Fig. 1. Two 'sandwich' systems; (a) the *a*-Si/Au(001)/*a*-Si, with a thickness of 40 Å for gold and 15 Å for each *a*-Si layers, (b) the strain-free model Si(001)[110] ||Au(001)[110]|| Si(001)[110] with a gold thickness of 40 Å in between two silicon layers of 33 Å. The inset is a zoom of the interface.

of the amorphous silicon phase, then we present two composite systems, the *a*-Si/Au(001)/*a*-Si 'sandwich' and the Au@*a*-Si core–shell NW. In order to evaluate the quality of our amorphous/crystalline interfaces, we also calculated and compared the interface and the adhesion energies of the strain-free model to the values obtained in amorphous silicon/crystalline gold interfaces.

3.1. Geometry

Amorphous Si preparation

The amorphous silicon phase was initially made by a random distribution of silicon atoms at the density of the diamond phase. An energy minimization was performed with the conjugate gradient algorithm until forces are smaller than 10^{-3} eV/Å to relax the highly stressed configurations. Then an annealing above the melting temperature of Si was run for 50 ps in the NPT ensemble. The system was cooled down at a quenching rate of 5.6×10^{13} K/s from 2800 K until 1 K and a final minimization with the conjugate gradient was applied until forces are lower than 10^{-6} eV/Å. This method was tested and validated in a previous study on diamond-Si@*a*-Si core–shell NWs [30].

a-Si/Au(001)/a-Si 'sandwich' system

Two *a*-Si films with a thickness of 15 Å were created on each side of the crystalline Au(001) film with the method defined previously (Fig. 1(a)). The gold film had a thickness of 40 Å. The Au atoms and the dimensions of the simulation box were frozen during the amorphous silicon preparation. Then the full system was annealed at 300 K in NPT ensemble during 5 ps in order to relax the interface.

Au@a-Si core–shell

A *a*-Si silicon cylindrical shell with a thickness of 20 Å was created around a [110] gold NW (Fig. 2), with the technique described here above. The core had a diameter of 70 Å and a length of 72 Å. It was maintained frozen during the shell preparation. An empty space of 1 Å was left between the core and the shell during the random filling of the shell to allow the atomic reconstruction of the interface. Once the amorphous phase was prepared, the full system was annealed at 300 K for 5 ps in NPT ensemble. We also considered the shell alone where the gold core was removed and the core alone without the shell (Fig. 2). Both were relaxed before additional mechanical tests were performed.

Strain-free Si(001)[110] ||Au(001)[110]|| Si(001)[110] 'sandwich' system

The Au(001) film is characterized by a 4:3 (Au:Si) coincidence site lattice along the in plane directions (Fig. 1(b)) [31]. The gold film shows a 0.06% tensile plane strain along [110] and [$\bar{1}$10] directions. The stresses along all directions of the 'sandwich' system are then completely relaxed.

3.2. Interface and adhesion energies of Au/Si systems

In order to evaluate the stability of the interfaces, we compared the interface and the adhesion energies of two Au/*a*-Si models: the sandwich (Fig. 1(c)) and the core–shell (Fig. 2), to those of the strain-free model (Fig. 1(b)). The adhesion energy E_{ad} corresponds to the energy required to separate the film from the substrate and it is defined as:

$$E_{ad} = (E_{Si} + E_{Au} - E_{Au/Si})/S$$

where E_{Si} and E_{Au} are the energy of the silicon substrate and the gold film alone after relaxation, $E_{Au/Si}$ the total energy of the relaxed Au/Si structure, and S the area of the interface. The interface energy E_{int} is related to E_{ad} by the relation of Dupré:

$$E_{ad} = E_{surf}^{Au} + E_{surf}^{Si} - E_{int}$$

where E_{surf}^{Au} and E_{surf}^{Si} correspond to the relaxed surface energies of the two newly formed surfaces when the film is separated from its substrate. The interface energy represents the excess energy introduced in the system due to the presence of the interface. It is indirectly dependent on the energy of the bulk phase via the adhesion energy (first equation), and corrected by the surface energies (second equation). For example, amorphous silicon had higher phase and surface energies than diamond silicon. As a consequence, the formation energy of an interface (E_{int}) in the crystalline strain-free model (001)Au/(001)Si (=1.25 J/m^2) was higher than in the sandwich amorphous/crystalline *a*-Si/(100)Au model (=0.33 J/m^2) (Table 3). However, the interface energies in the sandwich

Please cite this article in press as: J. Godet, et al., Uniform tensile elongation in Au–Si core–shell nanowires, Extreme Mechanics Letters (2016), http://dx.doi.org/10.1016/j.eml.2016.03.023

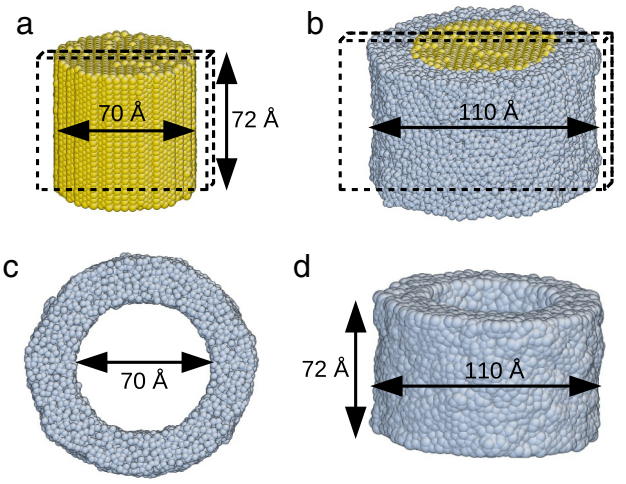

Fig. 2. (a) [110]Au pristine NW, (b) [110]Au@*a*-Si core–shell NW, (c) top and (d) front view of the empty *a*-Si shell. The boxes with dashed line correspond to slices cut in the NWs to observe the mechanisms of plasticity at the atomic scale (see Fig. 4).

Table 3
Excess interfacial energy E_{int} and adhesion energy E_{ad} for the strain-free model, the *a*-Si/(100)Au/*a*-Si (Fig. 1), and the [110]Au@*a*-Si core–shell NW (Fig. 2).

Interface	Strain-free	*a*-Si/(100)Au	[011]Au@*a*-Si
E_{int} (J/m^2)	1.25	0.33	0.20
E_{ad} (J/m^2)	1.51	1.55	1.53

model (*a*-Si/(100)Au) and in the [011]Au@*a*-Si core–shell NW, both containing an amorphous phase, differed by only 0.13 J/m^2. The differences could be related to the geometry cylindrical or planar.

Interestingly, the adhesion energies in the three systems were almost the same, close to 1.5 J/m^2 (Table 3). The energy required to separate the film from its substrate appeared then independent on the atomic configuration of the interface (amorphous or crystalline) and independent on the geometry (circular or planar).

We were not able to find any experimental reference for the interface and the adhesion energies. However our excess interface energies were about the same order of magnitude of crystalline Cu/Nb 0.82 J/m^2 [32], or crystalline Cu/W interface 0.83 J/m^2 [33]. We can also remark that the adhesion energy was less than two times the smaller surface energy calculated by our potential (here the (111) Au surface, see Table 1), it is then favorable to cleave the system along the interface plane rather than along the pure Au or the pure Si plane. Finally, we can note that the adhesion energies calculated in amorphous/crystalline interfaces were similar to the one calculated in epitaxial strain-free model, supporting the relatively good optimization of the amorphous interface configurations.

4. Mechanical properties of Au@*a*-Si core–shell NW

4.1. Results

In this part, we compare the stress–strain curves of the pristine Au NW alone, the empty *a*-Si shell and the Au@*a*-Si core–shell NW (Fig. 2) during a tensile test at 100 K (Fig. 3).

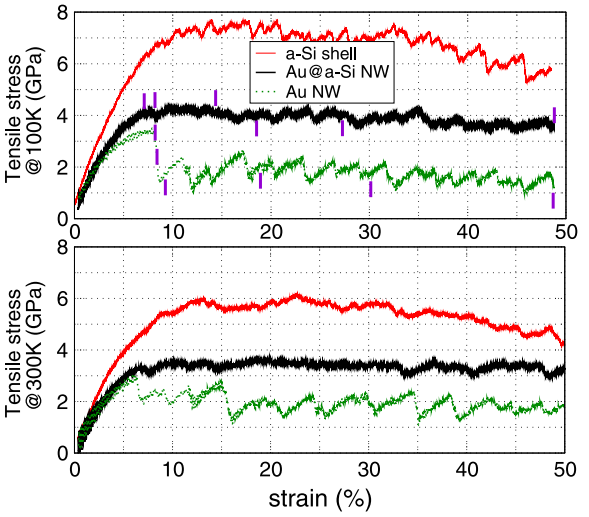

Fig. 3. True stress–true strain curves obtained under a tensile strain at 100 K (top panel) and 300 K (bottom panel) for the pristine [110]Au NW (green-dotted line), the empty *a*-Si shell (red line) and for the [110]Au@*a*-Si core–shell NW (black line). The vertical tick bars indicate the points where the snapshots on Fig. 4 have been extracted. (For interpretation of the references to color in this figure legend, the reader is referred to the web version of this article.)

All models showed a first linear elastic loading up to ∼3%, followed by a nonlinear elastic loading up to the first plastic events.

4.1.1. Pristine Au NW (100 K)

For Au NW, the first stress drop, observed at 8.21% on the stress–strain curve (Fig. 3; green-dotted curve), corresponds to the onset of plasticity. It corresponds to the nucleation of a leading partial dislocation loop along the $(11\bar{1})$ slip plane (Fig. 4; $\varepsilon = 8.21\%$). An avalanche of leading partial dislocation loops was subsequently nucleated from the surface step left by the first dislocation. This avalanche was at the origin of the gold twinning in the (111) planes (Fig. 4; $\varepsilon = 8.34\%$ and 9.18%). This mechanism operated

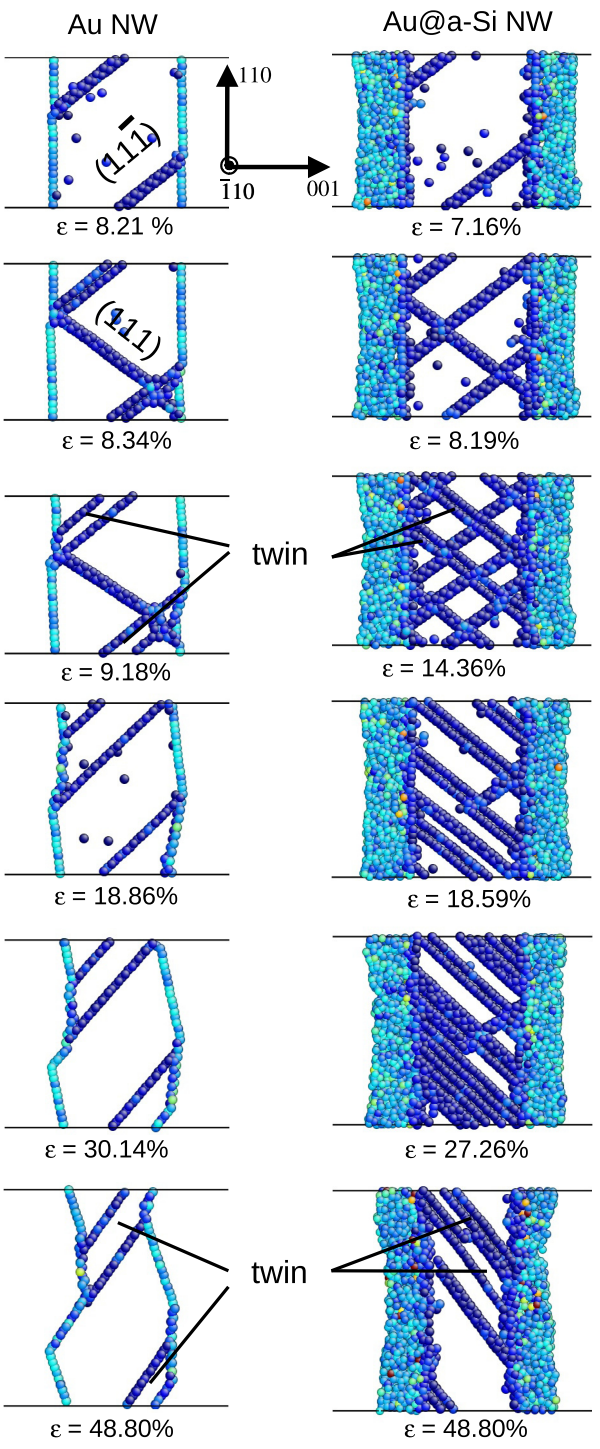

Fig. 4. Relevant stages of microstructures observed during plastic relaxation of the pristine Au NW (left panel) and the [110]Au@*a*-Si core–shell NW (right panel) subjected to a tensile strain at 100 K. Only the slices delimited by dashed lines on Fig. 2 are shown. The images are obtained with the centro-symmetry criterion that only shows the non FCC structures of Au crystal. The light blue spheres represent the surface atoms, the dark blue the atoms of the stacking faults. The strain of each snapshot are identified by a vertical tick on Fig. 3. (For interpretation of the references to color in this figure legend, the reader is referred to the web version of this article.)

during the same stress drop in order to relax the stress (Fig. 3). A succession of reloadings and plastic relaxations contributed to the twin growth, characterized by the saw-tooth shape of the stress–strain curve. At $\varepsilon = 18.86\%$, a trailing partial dislocation removed the stacking fault in the (111) plane, while new leading partial dislocation loops

Please cite this article in press as: J. Godet, et al., Uniform tensile elongation in Au–Si core–shell nanowires, Extreme Mechanics Letters (2016), http://dx.doi.org/10.1016/j.eml.2016.03.023

increased the thickness of the twin. Interestingly, the formation of gold twin has been obtained in experiments and in simulations performed on gold nanopillars under tensile strain [34], confirming the ability of the MEAM potential to describe the mechanical properties of gold. For larger strain, the twinning stopped, the stress was then relaxed by the nucleation of dissociated perfect dislocations along the twin boundary increasing the step height (Fig. 4; $\varepsilon = 30.14\%$ and 48.80%).

4.1.2. Isolated a-Si shell (100 K)

The isolated *a*-Si shell showed a quasi elastic behavior up to 8% (Fig. 3; red curve), despite some local atomic rearrangements characteristic of amorphous phase that can be partly identified by small peaks on the stress–strain curve. Then, the stress reached a plateau where the atomic rearrangements are more important up to about 35%. At 35%, we observed bond breaking leading to void formation in the shell. The softening on the stress–strain curve observed at larger strain corresponds to the void expansion (atomic configurations not shown here).

4.1.3. [110]Au@a-Si core–shell (100 K)

The core–shell NW presents a similar nonlinear elastic loading as in Au NW but can sustain higher stresses thanks to the hard *a*-Si shell (Fig. 3; black curve), in agreement with the mechanical properties of gold foam covered by a hard amorphous shell [5]. We noted that the initiation of the first plastic event in the core–shell (a leading partial dislocation) appeared at smaller strain ($\varepsilon = 7.16\%$) (Fig. 4) than in Au core alone ($\varepsilon = 8.21\%$). This was already observed in Si@*a*-Si core–shell NWs where the atomic configurations of the defects at the interface act as dislocation seeds favoring the onset of plasticity [30]. Here also, the interface defects can act as favorable dislocation sources that are absent of the surface of the pristine Au NW. At larger strains (Fig. 4; $\varepsilon = 14.36\%$), new leading partial dislocations were nucleated in both $(11\bar{1})$ and (111) planes, accompanied by trailing partial dislocations that removed almost all the stacking fault at larger strain (Fig. 4; $\varepsilon = 48.80\%$). Interestingly, very few twins were observed in core–shell NW unlike in Au NW. Moreover, when they were present, their extension was limited to 2 or 3 atomic planes. Finally, during the nucleation of the individual partial dislocations, the flow stress is almost constant for the strain in between 7% and 50%, which is characteristic of a perfect plastic behavior.

4.1.4. Results at 300 K

At 300 K, the stress–strain curves (Fig. 3) are similar to these obtained at 100 K. Overall, we observed a decrease of the yield points characteristic of the higher temperature. We can also point out the remarkable temperature sensitivity in *a*-Si shell. The flow stress was reduced by about 1.5 GPa when the temperature increased by 200 K, in agreement with another study using a different potential [35]. This effect seems to have a direct consequence on the flow stress of the core–shell that was almost 1 GPa lower at 300 K than at 100 K, while the flow stress in Au NW was almost equivalent at 100 and 300 K. Moreover, the roughness of the Au@*a*-Si stress–strain curve is smaller at 300 K than at 100 K. Both of these outcomes suggest that there are some very low barrier transitions that can be thermally activated at these strain rates at 300 K but not at 100 K. The microstructures in the core–shell observed at 300 K (not shown here) were relatively similar to those observed at 100 K (Fig. 4) with slightly larger twin bands in the core–shell NW up to 3 or 4 planes.

4.2. Discussion

4.2.1. Yield point and strain rate

The large yield strains obtained for the Au NW and the core–shell NW (about 7%–8% at 100 K and 6%–7% at 300 K (Fig. 3)) are higher than the experimental yield strain of a few % at 300 K [34]. The differences are related to several points. The very high strain rate used in simulations could overestimate the yield stress by almost a factor of two at 300 K [36]. The small overestimation of the ideal shear strength in gold (Table 1) could also impact the yield strength. With the absence of pre-existing dislocations and internal dislocation sources in our nanostructures, the dislocations must be nucleated from the surface which is also at the origin of the large yield stress. Moreover, the surface of our pristine Au NW is perfectly flat, no surface defects can help the dislocations nucleation at lower strain [37].

4.2.2. Amorphous-shell and interface effects

Concerning the mechanical behavior, the *a*-Si shell appears at the origin of the reduced incidence of twinning in the core–shell NWs. The geometry of the NW activates slip on two planes: the (111) and the $(11\bar{1})$ (Fig. 4). When the first dislocation glides across the metal core, it eventually reaches the Au–Si interface and forms a step on it. However, the hard Si shell exerts a back-stress on the step, initiating the nucleation of a second dislocation that erases the step at the interface. This new dislocation glides through the metal core along a different slip plane than the first dislocation. Thus, the hard amorphous shell works against the growth of the ledges left by localized plasticity and by consequence works against the expansion of nanotwins.

In pristine nanostructures, the nucleation of new dislocations at the surface was favored because of the kinetic energy locally released when a dislocation emerges at the surface. This mechanism is called kinetic dislocations emission [21]. It is at the origin of the dislocation avalanches associated to the abrupt drop in the saw-tooth shapes stress–strain curve of Au NW (Fig. 3). In our core–shell NW, this mechanism was not observed, as if the kinetic energy of the dislocation was absorbed by the amorphous shell. To summarize, while the interface defects favor the dislocation nucleation at the onset of plasticity, the subsequent plastic events require the same level of stress as the one required to nucleate the first plastic event, thanks to the presence of the hard amorphous shell. The latter is at the origin of the perfect plastic behavior observed in our core–shell NWs.

Please cite this article in press as: J. Godet, et al., Uniform tensile elongation in Au–Si core–shell nanowires, Extreme Mechanics Letters (2016), http://dx.doi.org/10.1016/j.eml.2016.03.023

4.2.3. NW orientation

The [011] orientation chosen in our simulations corresponds to the double slip mode for the plasticity which allows strong entanglement of dislocations in the core–shell NW (Fig. 4; $\varepsilon = 14.36\%$). However, the work hardening expected by such configurations was not observed or very little on the stress–strain curve (Fig. 3). This could be related to the fact that stacking faults alone or very thin twins are not efficient for strengthening conversely to nano-twin [38]. We can also note that the size of our nanostructures was very small, by consequence the yield stress is very high and close to the theoretical elastic limit. In our core–shell NWs, the overall plasticity then operates at stresses high enough to smooth the stress fluctuation due to the dislocation entanglement.

4.2.4. Geometry at large strain

A direct consequence of the core–shell architecture is the conservation of the cylindrical geometry at very large strain up to about 50% (Fig. 4). The hard shell prevents the localization of the deformation in a unique plane or in a limited zone as observed in pristine Au NW. It then favors the nucleation of dislocations all along the NW axis to homogeneously distribute the plastic deformation. The hard amorphous shell appears to preserve the geometry of the core–shell even after large plastic deformations.

5. Conclusions

We identified a MEAM parametrization for gold and silicon that we optimized with respect to the mechanical properties of pristine silicon, amorphous silicon and pristine gold. We fitted gold–silicon interactions on the B1 phase of Au–Si and on the energies of substitutional Si atom in pure Au and Au atom in pure Si. The adhesion energies in *a*-Si/Au interfaces are similar to those calculated in the strain-free interface, which suggests a relatively good quality of the *a*-Si/Au interfaces. The mechanical tests performed on Au@*a*-Si core–shell NW show few twins with very small extension whereas in pristine Au NW, the twins have a large extension. The hard amorphous shell acts as a barrier against the interface deformation due to localized plasticity but favors the homogeneous plastic deformation all along the NW. As a consequence, the core–shell can sustain very high plastic deformation of up to 50% without shape modification and almost no softening.

In conclusion, such core–shell nanostructures composed of a hard amorphous shell are able to support very high yield stress and could be used as elements for the building of hard architectured materials with low density. More investigations are still needed to support these results and to understand the role of other parameters such as cross section geometry, NW length, NW orientation or shell thickness.

Acknowledgments

We wish to thank the region Poitou-Charentes and 'l'Agence Nationale de la Recherche' for the financial support for this research under the grant reference ANR-12-BS04-0003-01, as well as Mathieu Loiseau for his support. This work pertains to the French Government program Investissements dAvenir (LABEX INTERACTIFS, reference ANR-11-LABX-0017-01).

Appendix A. Supplementary material

Supplementary material related to this article can be found online at http://dx.doi.org/10.1016/j.eml.2016.03.023.

References

[1] M. Ashby, Materials—A brief history, Phil. Mag. Lett. 88 (9–10) (2008) 749–755.
[2] N.A. Fleck, V.S. Deshpande, M.F. Ashby, Micro-architectured materials: past, present and future, Proc. R. Soc. Lond. A Math. 466 (2121) (2010) 2495–2516.
[3] T.A. Schaedler, A.J. Jacobsen, A. Torrents, A.E. Sorensen, J. Lian, J.R. Greer, L. Valdevit, W.B. Carter, Ultralight metallic microlattices, Science 334 (6058) (2011) 962–965.
[4] J.W.C. Dunlop, P. Fratzl, Multilevel architectures in natural materials, Scr. Mater. 68 (1) (2013) 8–12.
[5] M.M. Biener, J. Biener, A. Wichmann, A. Wittstock, T.F. Baumann, M. Baeumer, A.V. Hamza, ALD functionalized nanoporous gold: Thermal stability, mechanical properties, and catalytic activity, Nano Lett. 11 (8) (2011) 3085–3090.
[6] S. Ryu, C.R. Weinberger, M.I. Baskes, W. Cai, Improved modified embedded-atom method potentials for gold and silicon, Modelling Simul. Mater. Sci. Eng. 17 (7) (2009).
[7] K. Kang, W. Cai, Brittle and ductile fracture of semiconductor nanowires—Molecular dynamics simulations, Phil. Mag. 87 (14–15) (2007) 2169.
[8] S. Ryu, W. Cai, A gold–silicon potential fitted to the binary phase diagram, J. Phys.: Condens. Matter. 22 (5) (2008).
[9] B.-J. Lee, J.-H. Shim, M.I. Baskes, Semiempirical atomic potentials for the fcc metals Cu, Ag, Au, Ni, Pd, Pt, Al, and Pb based on first and second nearest-neighbor modified embedded atom method, Phys. Rev. B 68 (2003) 144112.
[10] B.-J. Lee, A modified embedded atom method interatomic potential for silicon, CALPHAD 31 (1) (2007) 95–104.
[11] S. Plimpton, Fast parallel algorithms for short-range molecular dynamics, J. Comput. Phys. 117 (1995) 1–19. URL: http://lammps.sandia.gov.
[12] S. Nosé, A unified formulation of the constant temperature molecular dynamics methods, J. Chem. Phys. 81 (1) (1984) 511–519.
[13] W.G. Hoover, Canonical dynamics: Equilibrium phase–space distributions, Phys. Rev. A 31 (3) (1985) 1695.
[14] M.I. Baskes, Modified embedded-atom potentials for cubic materials and impurities, Phys. Rev. B 46 (5) (1992) 2727–2742.
[15] F.H. Stillinger, T.A. Weber, Computer simulation of local order in condensed phases of silicon, Phys. Rev. B 31 (8) (1985) 5262.
[16] J. Tersoff, Modeling solid-state chemistry: Interatomic potentials for multicomponent systems, Phys. Rev. B 39 (8) (1989) 5566.
[17] G. Simmons, H. Wang, Single Crystal Elastic Constants and Calculated Aggregate Properties: A Handbook, second ed., MIT Press, Cambridge, MA, 1971.
[18] D.R. Lide (Ed.), CRC Handbook of Chemistry and Physics, CRC, Ann Arbor, 1991.
[19] C. Kittel, Introduction to Solid State Physics, eighth ed., John Wiley & Sons, Inc., New York, 2005.
[20] Y.-M. Juan, E. Kaxiras, Generalized stacking fault energy surfaces and dislocation properties of silicon: first-principle theoretical study, Phil. Mag. A 74 (6) (1996) 1367.
[21] J.P. Hirth, J. Lothe, Theory of Dislocations, second ed., Wiley, New York, 1982.

Please cite this article in press as: J. Godet, et al., Uniform tensile elongation in Au–Si core–shell nanowires, Extreme Mechanics Letters (2016), http://dx.doi.org/10.1016/j.eml.2016.03.023

[22] A.A. Stekolnikov, J. Furthmüller, F. Bechstedt, Absolute surface energies of group-iv semiconductors: Dependence on orientation and reconstruction, Phys. Rev. B 65 (2002) 115318.
[23] W. Tyson, W. Miller, Surface free energies of solid metals: Estimation from liquid surface tension measurements, Surf. Sci. 62 (1) (1977) 267–276.
[24] V. Vitek, Intrinsic stacking faults in body-centred cubic crystals, Phil. Mag. 18 (154) (1968) 773–786.
[25] W.-S. Ko, B.-J. Lee, Origin of unrealistic blunting during atomistic fracture simulations based on MEAM potentials, Phil. Mag. 94 (16) (2014) 1745–1753.
[26] K. Kang, W. Cai, Size and temperature effects on the fracture mechanisms of silicon nanowires: Molecular dynamics simulations, Int. J. Plast. 26 (9) (2010) 1387–1401.
[27] K. Laaziri, S. Kycia, S. Roorda, M. Chicoine, J.L. Robertson, J. Wang, S.C. Moss, High resolution radial distribution function of pure amorphous silicon, Phys. Rev. Lett. 82 (1999) 3460–3463.
[28] K. Laaziri, S. Roorda, J. Baribeau, Density of amorphous SixGe1-x alloys prepared by high-energy ion implantation, J. Non-Cryst. Solids 191 (1–2) (1995) 193–199.
[29] S. Roorda, W.C. Sinke, J.M. Poate, D.C. Jacobson, S. Dierker, B.S. Dennis, D.J. Eaglesham, F. Spaepen, P. Fuoss, Structural relaxation and defect annihilation in pure amorphous silicon, Phys. Rev. B 44 (1991) 3702–3725.
[30] J. Guénolé, J. Godet, S. Brochard, Plasticity in crystalline-amorphous core–shell Si nanowires controlled by native interface defects, Phys. Rev. B 87 (2013) 045201.
[31] M. Woelz, Y.-L. Huang, M. Seibt, S.C. Erwin, Epitaxial growth of gold on Si(001), Surf. Sci. 624 (2014) 15–20.
[32] M. Demkowicz, L. Thilly, Structure, shear resistance and interaction with point defects of interfaces in Cu–Nb nanocomposites synthesized by severe plastic deformation, Acta Mater. 59 (20) (2011) 7744–7756.
[33] A. Ruffini, J. Durinck, J. Colin, C. Coupeau, J. Grilhé, Gliding at interface during thin film buckling: A coupled atomistic/elastic approach, Acta Mater. 60 (3) (2012) 1259–1267.
[34] S. Lee, J. Im, Y. Yoo, E. Bitzek, D. Kiener, G. Richter, B. Kim, S.H. Oh, Reversible cyclic deformation mechanism of gold nanowires by twinning-detwinning transition evidenced from in situ TEM, Nature Commun. 5 (2014) 3033.
[35] M.J. Demkowicz, A.S. Argon, Autocatalytic avalanches of unit inelastic shearing events are the mechanism of plastic deformation in amorphous silicon, Phys. Rev. B 72 (2005) 245206.
[36] T. Zhu, J. Li, A. Samanta, A. Leach, K. Gall, Temperature and strain-rate dependence of surface dislocation nucleation, Phys. Rev. Lett. 100 (2) (2008) 025502.
[37] P. Hirel, J. Godet, S. Brochard, L. Pizzagalli, P. Beauchamp, Determination of activation parameters for dislocation formation from a surface in fcc metals by atomistic simulations, Phys. Rev. B 78 (6) (2008) 064109.
[38] D. Jang, X. Li, H. Gao, J.R. Greer, Deformation mechanisms in nanotwinned metal nanopillars, Nature Nanotechnol. 7 (9) (2012) 594–601.

Please cite this article in press as: J. Godet, et al., Uniform tensile elongation in Au–Si core–shell nanowires, Extreme Mechanics Letters (2016), http://dx.doi.org/10.1016/j.eml.2016.03.023